Magnetic Resonance Imaging of Immiscible-Fluid Displacement in Porous Media

Jing-Den Chen,[1] Madalena M. Dias,[1,3] Samuel Patz,[2] and Lawrence M. Schwartz[1]
[1]*Schlumberger-Doll Research, Old Quarry Road, Ridgefield, Connecticut 06877-4108*
[2]*Radiology Department, Brigham and Womens Hospital, Harvard Medical School, Boston, Massachusetts 02115*
[3]*Schlumberger Cambridge Research, P. O. Box 153, Cambridge CB30HG, United Kingdon*
(Received 30 November 1987)

Magnetic resonance imaging is used to study oil and water invasion in a model porous medium. Images taken normal to the flow direction are processed to give both the oil saturation and the fractal character of the oil distribution. These images reveal qualitative differences between the cases of invasion by the wetting (water) and nonwetting (oil) fluids. We have also found large saturation fluctuations in the residual oil state in which the oil consists entirely of disconnected blobs.

PACS numbers: 47.55.Mh, 47.55.Kf, 61.16.Hn, 68.70.+w

Recently authors have devoted considerable attention to patterns formed by fluid invasion in porous media.[1] Much of this work has been carried out in two dimensions where the displacement front is visible and therefore readily analyzed.[2-5] The situation in three dimensions is clearly more complicated. By index matching the fluids to the porous matrix one can, in effect, look inside a solid material to study the invasion process.[6] This approach is, of course, limited to very special choices of the fluids and solids. An alternative approach is to evaluate the flow process *destructively*. In a recent paper[7] Wood metal, and alloy that melts at 70 °C, was used as the invading fluid; the system was then cooled below the alloy's melting temperature and the flow patterns examined in successive slices. While this approach allows the study of invasion patterns with pore scale resolution, one is again limited to a narrow choice of materials and, of course, to a single flow experiment in each porous host. In the present paper we describe the application of magnetic resonance tomography to the study of immiscible-fluid displacement.[8,9] The advantages of tomography are the following: (1) It is a nondestructive technique; (2) there are no inherent limitations on the choice of fluids; and (3) the invasion patterns can, in principle, be studied while flow is in progress. Our experiments are based on homogeneous synthetic porous media and involve resolutions that are close to the pore and grain length scale. We will show that consistent processing of the digitized tomographic images provides a reasonable basis for the description of displacement patterns and allows us to distinguish between the profiles formed by different flow sequences.

The porous medium employed in this work was comprised of unconsolidated crushed Pyrex particles. The grains were sieved to a size distribution between 420 and 500 μm, cleaned by hand (to remove opaque particles), washed with 20 wt.% HCl solution, and rinsed with deionized water. After oven drying, the grains were packed into a cylindrical Plexiglas tube whose length and inner diameter are 23.5 and 6.3 cm, respectively. The final porosity of the packing was measured volumetrically to be 0.45. The fluids used in the flow experiments were (1) an aqueous solution comprised of 44.77-gm $NiSO_4 \cdot 6H_2O$ per 1000 ml of deionized water and (2) Soltrol 100 (an isoparaffin oil) which was dyed blue to improve visualization. The Ni^{++} ions suppress the NMR signal from the water so that our images are sensitive to just the oil distribution. The density of the aqueous solution is 1.025 g/cm^3 and its viscosity is 1.06 cP. The corresponding numbers for Soltrol 100 are 0.737 g/cm^3 and 1.02 cP. The interfacial tension, γ, between the two fluids was 38.8 dyn/cm and the experiments were run at room temperature (23-24 °C). The measurement sequence is indicated schematically in Fig. 1. In its initial state, the vessel was saturated with the aqueous solution. Oil was flowed into the vertical core from above until an invasion front was visible at roughly the midpoint of the sample. This process, in which we have invasion by the *nonwetting* fluid, is referred to as *drainage*. The flow was then stopped and a series of images made with the image plane normal to the flow direction. (During this process several images were re-

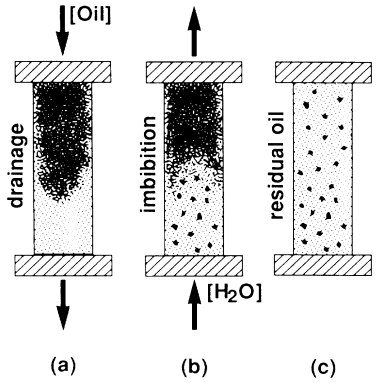

FIG. 1. Schematic representation of the experimental sequence: drainage → irreducible water → imbibition → residual oil.

© 1988 The American Physical Society

peated to check that there was no rearrangement of the oil distribution.) The oil flow was then continued at a high flow rate until no additional water was produced at the lower end of the containing vessel. In this *irreducible water* state the oil saturation, S_o, was measured (by a comparison of initial and final weights) to be 0.846. We considered next the process of *imbibition,* i.e., invasion by the wetting phase. The aqueous solution was flowed in from below until a front was evident near the middle of the sample. A second series of images (again, normal to the flow direction) was made through the front and the displacement was then resumed until only water was produced at the top of the vessel. The *residual oil* remaining at the end of this process is comprised of disconnected blobs which cannot be moved by the flowing water. The volumetrically measured oil saturation in this state is $S_o \approx 0.107$. A series of images of these oil blobs was taken in order to study the variation in the residual oil saturation. For both the drainage and imbibition experiments the capillary number, C_a, was estimated to be $\approx 6.6\times 10^{-9}$. [$C_a \equiv \mu v/\gamma$, where μ is the viscosity of the displacing fluid and $v = q/A$ is the superficial velocity (q is the volumetric flow rate and A is the cross-sectional area of the core).] The corresponding Bond number is $B_0 \approx 0.0045$. [$B_0 \equiv (\delta\rho)gR^2/\gamma$, where $\delta\rho$ is the density difference, g is the gravitational constant, and R is a typical pore radius.] At such a low capillary number viscous effects are negligible and the displacement process is controlled by gravity and capillarity. The transition length of the flood interface can be estimated as $\delta l \approx R/B_0 \approx 6$ cm, a value consistent with our laboratory observations. Note that in the work of Ref. 7, where the two fluids were the molten and vapor phases of Wood metal, the length of the invasion front was roughly a factor of 10 smaller than in our experiments.

Our tomography was based on a Carr-Purcell spin-echo method combined with a standard two-dimensional Fourier-transform technique. Proton NMR images were obtained at 1.9 T in a 31-cm bore Oxford superconducting magnet. A slice selection gradient was applied during the initial 90° frequency-selective rf pulse. Transverse dephasing during the selective rf pulse was rephased by reversal of the slice selection gradient. A single spin echo was recorded and the echo time, T_E, varied between 33 and 41 ms after the initial excitation of the spins. The maximum gradient strength available from each of the x, y, and z gradient coils was 1 G/cm. In a typical image, 256 phase encode values were collected and each was averaged six times with a 1-s recycle delay (for T_1 relaxation). The resulting 256×256 image requires 26.5 min of data collection. For each spin echo, 256 complex points were recorded with a typical dwell time of 40 μs and the dimensions of an image voxel were usually 0.45×0.45 mm^2 in the plane of the image and 1.7 mm perpendicular to this plane.

Consider next the processing of the flow images. A typical grey-scale display, shown in Fig. 2, indicates that the oil is distributed throughout the image plane in a complex pattern. Since the brightness of each pixel (which varies between 0 and 255) is proportional to the oil density, a sum over all pixels yields the product of the porosity, ϕ, and S_o.[10] In practice, the image processing is always complicated by a certain level of low-intensity noise. We have filtered this noise by setting equal to

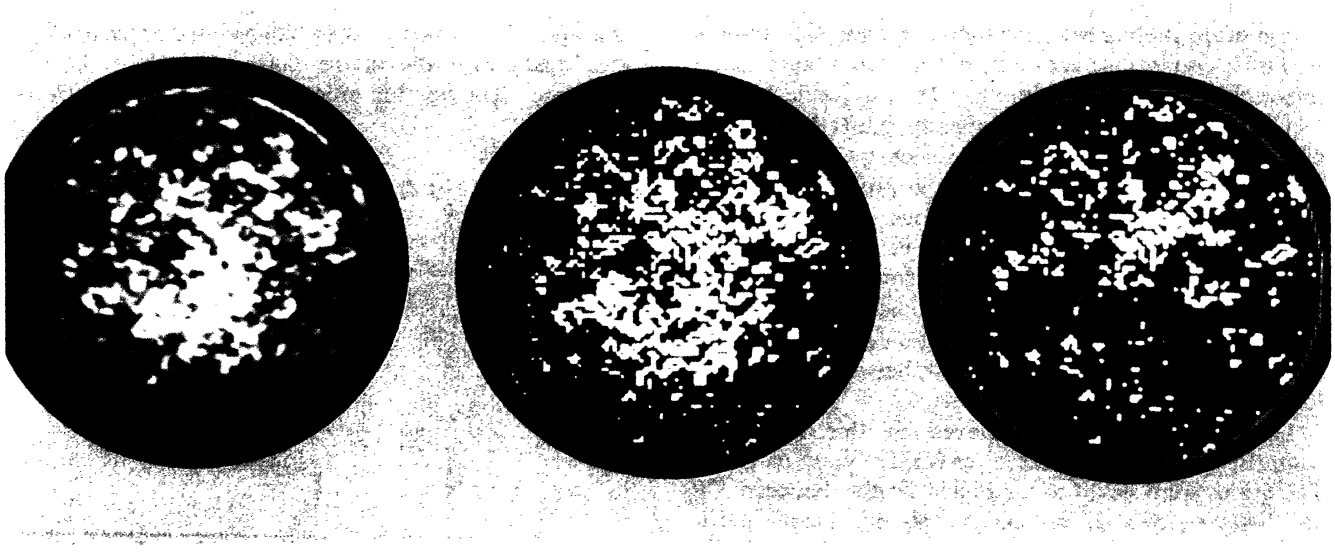

FIG. 2. Typical grey-scale (left) and binary (center) representations of one of the imbibition images. In the right-hand panel, clusters are coded by size: 1–9 (white), 10–20 (red), 21–43 (yellow), 44–65 (green), 66–90 (cyan), 91–110 (blue), and 111–125 (magenta).

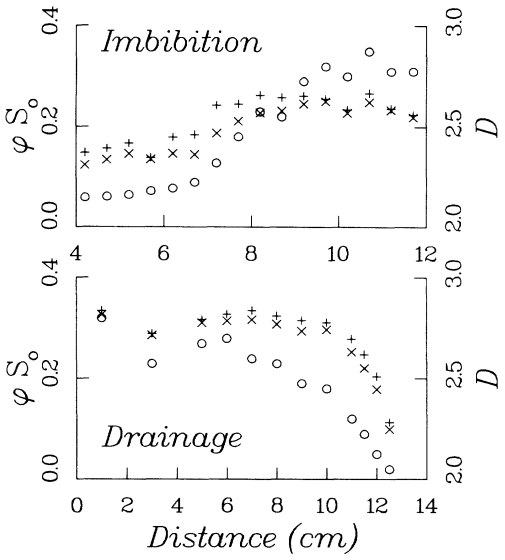

FIG. 3. Oil saturation S_o (open circles) plotted as a function of depth (measured from the *inflow* end) for drainage and imbibition. Also shown are the values of the fractal dimension obtained from the full grey-scale (plusses) and binary (crosses) images.

zero the intensity of all pixels whose brightness is below a minimum cutoff whose value is chosen to blacken the region outside of the circular core cross section. This procedure was tested on a fully saturated calibration core with $\phi S_o = 0.430$; the corresponding value obtained from the image was $\phi S_o = 0.415$. While this level of agreement is quite satisfactory, we have found that at low oil saturations the computed values of S_o are rather sensitive to the threshold used to eliminate the background noise. Accordingly, our saturation profiles should be viewed as providing a semiquantitative description of the oil distribution. In Fig. 3 we show the variation of S_o along the cylinder axis for the drainage and imbibition experiments. The sharp cutoff in the drainage curve reflects the fact there is a point beyond which the invading oil does not penetrate. By contrast, in imbibition the invading water leaves behind blobs of residual oil and the saturation shows a steplike profile. Once S_o has been calculated, we can reduce the grey-scale image to a binary display of the same distribution (Fig. 2). We simply rank the pixels in order of increasing brightness, set pixels at the top (bottom) of the distribution equal to 1 (0), and choose the effective midpoint to guarantee that the binary and grey-scale images yield the same S_o. We see that the simpler binary image retains the essential structure of the oil distribution, while having the advantage of allowing us to study such issues as the distribution of connected oil clusters within the image plane (Fig. 2).

How can we characterize the geometry of the oil distribution as a function of depth into the displacement front? Beginning with the original grey-scale displays,

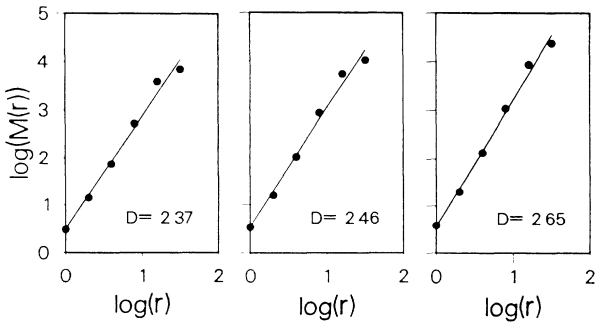

FIG. 4. Typical results for $M(r)$ vs r for the grey-scale images. Beginning at the left, the image planes are 4.2, 6.7, and 8.7 cm from the inflow end of the vessel.

let us choose a random point within the image and ask how much oil is contained within a circle of radius r centered at this point. (Clearly, the closer the center point is to the edge of the image, the smaller will be the allowed range of r values.) Averaging over many (typically 100) random centers we obtain the physically relevant distribution, $m(r)$. Rather than working directly with $m(r)$, for the purposes of a logarithmic display it is more convenient to look at $M(r) \equiv \sum_r^{2r-1} m(r)$. In Fig. 4 the behavior of $M(r)$ is shown at three depths for grey-scale imbibition images. Two features of this figure are worth noting. First, we see that over a range slightly greater than one decade in r, $M(r)$ exhibits the kind of power-law behavior characteristic of a fractal distribution. Second, it is clear that the fractal dimension, D, increases as the image plane moves through the invasion front. [The corresponding fractal dimension for $m(r)$ equals $D-1$.] In Fig. 3 the behavior of D as function of position along the cylinder axis is shown for the drainage

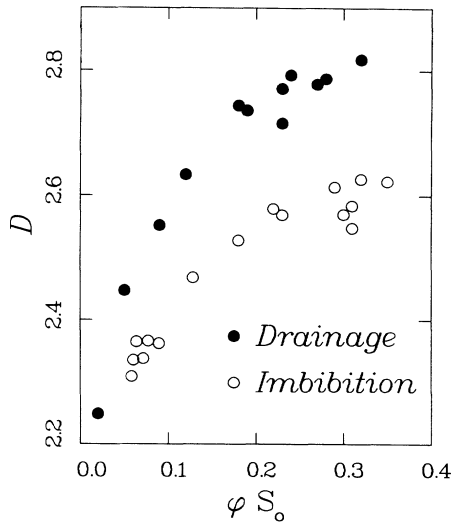

FIG. 5. Cross plots of ϕS_o and D (from binary images) for drainage and imbibition.

and imbibition images. (As expected, the sparser binary images are seen to yield slightly lower fractal dimensions than their grey-scale counterparts.) It is gratifying to see that both the grey-scale and binary values of D exhibit the same qualitative trends as S_o. It should be noted, however, that the results described here are rather different from those to be expected based on the theory of invasion percolation in the presence of buoyancy effects.[11] For example, in drainage, percolation theory predicts an oil cluster characterized by a *single* fractal dimension, D, and a correlation length, ξ, that varies along the invasion axis. A slice through the cluster should then show $m(r) \sim r^{D-1}$ $(r \leq \xi)$ and $m(r) \sim r^2$ $(r \geq \xi)$. We found, however, that it was not always possible to make this separation. (In many images the value of D appeared to depend on the choice of ξ.) Thus, the data by themselves did not suggest that the *same* fractal dimension should be used to describe each image.

Figure 3 illustrates that there are important differences between the drainage and imbibition profiles. This point is reinforced in Fig. 5 where we have cross plotted ϕS_o vs D for the two invasion processes. Clearly, at each oil saturation, the drainage values of D are higher. This reflects the fact that the imbibition front contains isolated residual oil blobs which lead to sparser images and lower values of D. We emphasize that the fact that drainage and imbibition lead to nonoverlapping distributions (in Fig. 5) implies that the value of D is *not* simply determined by S_o (as it would be in the case of points randomly thrown within a finite circle) but is a function of the flow process that generated the image.

Finally, we consider the residual oil distribution. Six images were taken in this state and the resulting values of ϕS_o were 0.038, 0.041, 0.052, 0.028, 0.050, and 0.070.[12] Surprisingly, these values show variation by more than a factor of 2. This suggests that one must average over distances on the order of a centimeter (i.e., roughly 6 times the image thickness) to obtain values of S_o characteristic of the bulk core. This is, in fact, supported by the analysis of preliminary multislice images.

The authors gratefully acknowledge important conversations with R. Lenormand, M. Lipsicas, and J. Willemsen.

[1]G. M. Homsy, Ann. Rev. Fluid Mech. **19**, 271 (1987).

[2]J. P. Stokes, D. A. Weitz, J. P. Gollub, A. Dougherty, M. O. Robbins, P. M. Chaiken, and H. M. Lindsay, Phys. Rev. Lett. **57**, 1718 (1986).

[3]G. Daccord, J. Nittmann, and H. E. Stanley, Phys. Rev. Lett. **56**, 336 (1986).

[4]J. D. Chen and D. Wilkinson, Phys. Rev. Lett **55**, 1892 (1985).

[5]R. Lenormand and C. Zarcone, Phys. Rev. Lett. **54**, 2226 (1985).

[6]J. D. Chen and N. Wada, Exp. Fluids **4**, 336 (1986).

[7]E. Clement, C. Baudet, E. Guyon, and J. P. Hulin, J. Phys. D **20**, 608 (1986).

[8]H. Vinegar, J. Pet. Technol. **38**, 257 (1986).

[9]L. D. Hall and V. Rajanayagam, J. Magn. Reson. **74**, 139 (1987).

[10]This saturation estimate depends on the lifetimes, T_1 and T_2, being independent of the size of the pore in which the oil resides. Physically, this assumption is reasonable in water-wet systems where the protons in the oil are effectively insulated from direct interactions with the grain surfaces. This point has been checked experimentally on oil-saturated water-wet packings with a range of grain sizes.

[11]D. Wilkinson, Phys. Rev. A **34**, 1380 (1986).

[12]The thresholds for these images have been set to give the correct average oil saturation. The variation in S_o, of interest here, is insensitive to the threshold position.

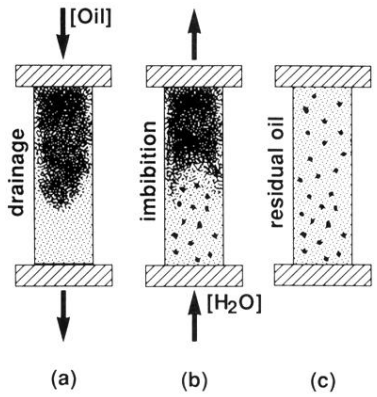

FIG. 1. Schematic representation of the experimental sequence: drainage → irreducible water → imbibition → residual oil.

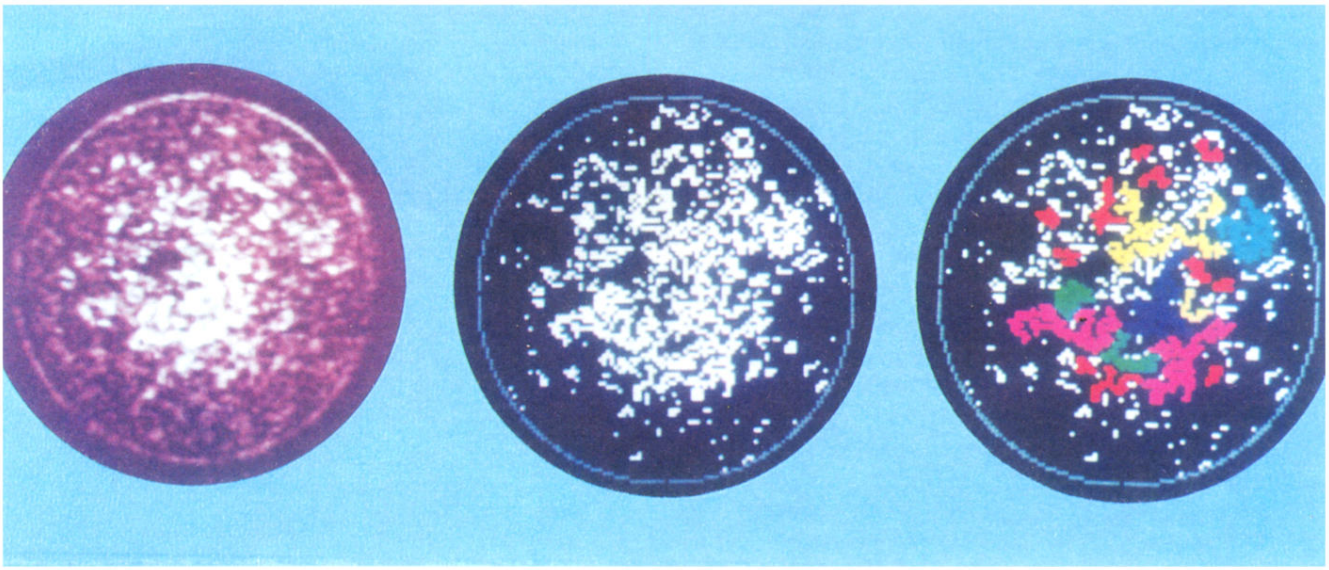

FIG. 2. Typical grey-scale (left) and binary (center) representations of one of the imbibition images. In the right-hand panel, clusters are coded by size: 1–9 (white), 10–20 (red), 21–43 (yellow), 44–65 (green), 66–90 (cyan), 91–110 (blue), and 111–125 (magenta).